Q. J. R. Meteorol. Soc. (1997), **123**, pp. 2297–2324

Thermodynamical impact and internal structure of a tropical convective cloud system

By F. GUICHARD*, J.-P. LAFORE and J.-L. REDELSPERGER
Centre National de Recherches Météorologiques, France

(Received September 1996; revised February 1997)

SUMMARY

A three-dimensional cloud-resolving model is used to simulate a cloud system, observed during the Tropical Ocean/Global Atmosphere Coupled Ocean–Atmosphere Response Experiment, corresponding to the development of shear parallel convective lines and characterized by the absence of large-scale ascent. The system life cycle includes different types of clouds interacting in both space and time.

The thermodynamical impact as well as statistical properties of the system are analysed using a partition of the total domain into several (6 to 12) internal areas. In-cloud temperature excess is weak as observed, whereas water vapour excess is significant and correlated with vertical velocity. However, buoyancy deviations are extremely small, indicating an equilibrium of density, involving thermodynamics and microphysics. Decomposition of budgets highlights the mechanisms of compensation occuring between the precipitating system and its environment.

Moisture convective transports are extremely intense and complex to analyse. A decomposition into vertical and horizontal parts shows that horizontal exchanges are important, in particular to explain moistening at upper levels. The effective part of vertical fluxes (after removing the compensating parts) occurs in active shallow and deep clouds, at very fine scales. These results question some basic hypotheses assumed in existing convective parametrizations.

KEYWORDS: Cloud-resolving model Convection Thermodynamical impact

1. INTRODUCTION

Cloud processes are a major element of the climatic system, involving in-cloud latent-heat release and precipitation as well as cloud–radiation interactions and convective vertical transport of water vapour. These small-scale transient features also represent a cause of great uncertainties in the understanding of climate dynamics and its response to a modification such as doubling CO_2 (Lindzen 1990; Betts 1990). In effect, cloud processes correspond to subgrid parametrized processes for large-scale models, and the latter appear very sensitive to the schemes that are used (Cess *et al.* 1990).

There are several explanations for this. Amongst them can be noted the lack of present knowledge concerning moist convection initiation (when and why does convection occur?), the way it interacts with the large-scale flow and its tendency toward organized mesoscale cloud systems. This leads to delicate problems for parametrization in terms of criteria for convection triggering, the choice of closure scheme and scale separation.

Convection schemes aim to parametrize modifications of temperature and water vapour fields due to cumulus convection. Some of them also determine the momentum transport by convection, or high-anvil generation (Tiedtke 1993). They have been tested and validated using existing observations, in particular with data from the Global Atmospheric Research Programme Atlantic Tropical Experiment (Lord 1982; Bougeault 1985; Tiedtke 1989). With observations alone, however, the different contributions of the various processes involved cannot be quantified. It is now possible to simulate explicitly an entire cloud system with cloud-resolving models (CRMs). Thus, CRMs appear now as useful tools, and complementary to observations for this problem, allowing one to further investigate cloudy processes and their parametrization.

CRMs have been extensively developed and used during the last fifteen years to study cloud systems. Several studies have been carried out with CRMs to determine the

---

* Corresponding author: Centre National de Recherches Météorologiques (CNRS and Météo–France), 42 avenue de Coriolis, 31057 Toulouse Cedex, France.

thermodynamical and dynamical impact of simulated convective systems on their large-scale environment, and to analyse the relative importance of the processes involved and their interactions. Non-precipitating shallow cumuli associated with trade wind regimes have been the first systems to be numerically studied, compared with observations and used to test, validate and improve parametrizations (Sommeria 1976, Sommeria and LeMone 1978, Siebesma and Cuijpers 1995 and others). Concerning deep convection, such studies have mainly focused on fast moving squall lines organized perpendicular to a moderate to strong wind shear (Tao and Simpson 1989, Caniaux *et al.* 1994), because these cloud systems exhibit a relatively well defined spatial structure. A decomposition of their total impact has highlighted the significant contributions of both the convective and stratiform parts of squall lines, in general agreement with observations (Johnson 1984, Chong and Hauser 1990). Nevertheless these studies only consider the mature quasi-permanent stage of such systems. The initial and dissipating stages are not simulated and analysed, whereas their impact at larger scales cannot be neglected.

A few studies have been devoted more closely to parametrizations of convection, such as those of Gregory and Miller (1989), Xu and Arakawa (1992) Xu *et al.* (1992), Xu (1994) and Xu (1995). Although these studies all use CRMs their approaches are, nevertheless, very different and the questions they raise quite distinct. For example, Xu and Arakawa (1992) focus on the problem of mesoscale organization, and show how CRM-derived data can be used, in an analogous way to observational data, to test a cumulus parametrization; the study of Gregory and Miller (1989) is concerned with basic hypotheses that are made in convection schemes. More precisely, Gregory and Miller (1989) decompose their domain of simulation into cloudy and clear-sky areas, as is done for cloud mass flux schemes, in order to derive a complete expression for the total impact of a cloud ensemble. The comparison of their full derivation with the approximate form that is used in convection schemes shows significant differences, mainly for water vapour. It seems necessary to include other terms, generally neglected in parametrizations of convection, for a good estimation of the impact of cumulus on water vapour.

Continuing from these previous studies, this paper focuses on the thermodynamical impact of a cloud system simulated explicitly. This case-study corresponds to the development of convective lines, observed during the Tropical Ocean/Global Atmosphere Coupled Ocean–Atmosphere Response Experiment (TOGA-COARE), oriented approximately parallel to a moderate low-level shear. Although these kinds of convective systems have not yet been intensively studied, they appeared to be very common during TOGA-COARE (cf. the summary report of the TOGA-COARE International Data Workshop) over the western equatorial Pacific, where the wind shear is often weak. A characteristic of this system is the absence of large-scale ascent (as analysed from the European Centre for Medium-Range Weather Forecasts (ECMWF) fields) and of the complex interactions with other convective clouds. Hence this is a specific case where convection occurs without the presence of large-scale convergence. In such a case convection schemes using a closure on the large-scale convergence of moisture would fail to capture this convective event.

This case has been chosen so as to study the mechanisms involved in convective organization where large-scale forcing is negligible. The 3D CRM develops convection by itself, starting from small random perturbations of temperature, thus avoiding the artificial initialization by a cold or warm perturbation that is often used. A realistic simulation of a cloud population is obtained, including different types of clouds (shallow to deep), over 10 hours of the model's life cycle.

We focus here on the way convection happens, not why it happens, in an approach similar to Gregory and Miller (1989). They separated heat and moisture budgets of their 2D simulations into two parts corresponding to the cloudy and clear-air regions. The main difference from their work is that we split the system into a greater number of internal areas, including convective and stratiform (less intense) precipitation areas as well as shallow-cloud areas, anvil-cloud areas and clear-sky columns. The simulation is analysed using this decomposition of the domain. First, statistical properties are presented; then, the contributions of different internal areas to the total cloud ensemble impact are analysed, and complete budgets over these areas are discussed. Thus, from a complex cloud ensemble we come to a simpler and more understandable system, formally analogous to 1D cloud-model types that are used in mass flux convection schemes.

The CRM, the budget equations and the partitioning method are presented in section 2. Section 3 briefly describes the main features of the simulation. The characteristics of internal areas are analysed in section 4. Thermodynamical budgets are discussed in section 5 and convective transport is further analysed in section 6.

2. METHODOLOGY

(*a*) *The cloud-resolving model*

We use the anelastic non-hydrostatic cloud model of Redelsperger and Sommeria (1986). It has been extensively used over a wide range of scales to represent squall lines (Lafore *et al.* 1988), frontal systems (Redelsperger and Lafore 1994) and shallow convection.

Model prognostic variables are the three components of the wind, u, v and w, the potential temperature θ, the specific humidity q_v, mixing ratios for five hydrometeor species (cloud liquid droplets q_c, rain drops q_r, ice crystals q_i, aggregates q_n and graupel q_h) and the subgrid turbulent kinetic energy e_t.

A Kessler-type parametrization is used for warm microphysical processes, except for subgrid-scale condensation and conversion from cloud droplets into rain drops (Redelsperger and Sommeria 1986). Ice-phase microphysics is dealt with by the scheme developed by Caniaux *et al.* (1994). Special care has been given to the formulation of parametrized turbulent processes. Based on a prognostic equation for e_t, it uses quasi-conservative variables for condensation and incorporates the effect of thermal stratification on subgrid fluxes (Balaji and Redelsperger 1996). Radiative effects are computed fully interactively with the cloud field using the radiation scheme of the ECMWF (Morcrette (1991), see Guichard *et al.* (1996) for its implementation in the CRM). Surface fluxes are expressed, following Louis (1979), with a sea surface temperature of 29.2 °C and a roughness length of 3×10^{-4} m.

(*b*) *Temperature and water vapour equations*

Equations of evolution of θ and q_v will be extensively used hereafter. They are expressed by:

$$\frac{\partial \theta}{\partial t} = -\frac{1}{\rho_0}\frac{\partial}{\partial x_j}\rho_0 \theta u_j + D_\theta + \frac{1}{\pi_0}Q^* + \frac{1}{\pi_0}Q_R + \left(\frac{\partial \theta}{\partial t}\right)_{LS} \tag{1}$$

$$\frac{\partial q_v}{\partial t} = -\frac{1}{\rho_0}\frac{\partial}{\partial x_j}\rho_0 q_v u_j + D_{q_v} - \frac{c_p}{L_v}Q + \left(\frac{\partial q_v}{\partial t}\right)_{LS}. \tag{2}$$

In these equations ρ is the density, c_p the specific heat at constant pressure, L_v the latent heating horizontally averaged over the simulation domain, $\pi = T/\theta$ the Exner function, D_θ and D_{q_v} represent the subgrid-scale turbulence for θ and q_v respectively. Subscript

0 refers to the anelastic base state, only depending on height. Q_R is the net radiative heating rate (solar and infrared), Q^* the total latent-heat release, including condensation, sublimation and fusion, whereas Q refers only to vapour-heat release (i.e. condensation and sublimation). The difference between terms Q^* and Q is generally small and corresponds to the ice-phase contribution through net fusion. Subcript LS refers to large-scale advection, however this forcing term vanishes for the present cloud system study and will be omitted hereafter, as large-scale convergence was found to be negligible in this particular case.

(*c*) *Partitioning the system into different internal areas*

The system under study typically includes areas of intense convective activity as well as clear-sky columns. The global budgets, at the domain-scale, are important, as they give the total impact of convection and the contribution of acting processes. Nevertheless, they only contain indirect information on what happens inside the domain. With a partition of the total domain into different internal areas, it is possible to get statistical information on the cloud ensemble, such as the intensity of convective draughts or the relative contribution of stratiform areas.

An additional reason for splitting the domain concerns mass flux schemes of convection. In effect, these parametrizations are based on a similar decomposition of the large-scale grid box. They assume that columns consist of restricted convective areas surrounded by a quiet environment, and make assumptions about the behaviour of this system (Arakawa and Schubert 1974; Tiedtke 1989)

Lipps and Hemler (1986) and Tao and Simpson (1989) have pursued such statistical analysis of simulated deep-cloud ensembles, using a method of partitioning based on a distinction between clear and cloudy areas. For cloudy areas they also differentiate between updraught and downdraughts, and thus come to a detailed description of the cloud ensemble. Gregory and Miller (1989) and Krueger (1988) used a similar kind of partition. The decomposition of Gregory and Miller also included complex terms due to the fact that cloud area (σ_C) varies with height and in time. Our partition of the domain differs from these previous studies in that we define criteria distinguishing entire columns (i.e. no height dependency, as in Xu (1995)), and we consider a large number of internal areas (A_i).

Table 1 summarizes the criteria used to define six basic internal areas. We distinguish between three regions with precipitation A_1, A_2, A_3, collectively A_p: A_1 comprises convective precipitation regions, also referred to as A_{p_c}; A_2 refers to stratiform precipitation areas, and A_3 to areas of trailing precipitation not reaching the ground—together A_2 and A_3 are referred to as A_{p_s}. We also have three non-precipitating environments A_4, A_5, A_6, collectively A_{np}: A_4 comprises shallow clouds, also referred to as A_{sh}; A_5 refers to areas of icy anvils, and A_6 to clear-sky columns—together A_5 and A_6 are referred to as $A_{a.s}$. Figure 1 illustrates the different regions.

Following Tao and Simpson (1989), A_{p_c} is defined as the ensemble of columns satisfying one of the two conditions: surface rainfall rate is greater than 20 mm h^{-1}, or greater than 4 mm h^{-1} and twice as large as the average value taken over the 24 surrounding grid points; in this last case the 8 closest surrounding columns are also retained as part of A_{p_c}. The shallow-convection area A_{sh} definition is based on Sui *et al.* (1994). Each internal area can be further split into updraught and downdraught sub-ensembles, so that up to 12 internal areas can be considered for some applications (see section 6). The above criteria are applied at each model time step.

TABLE 1. CRITERIA USED TO DEFINE AT EACH MODEL TIME STEP THE 6 BASIC INTERNAL AREAS.

Internal areas			Name	Criteria	References
Precipitating system (A_p)	A_{pc}	A_1	convective areas	$R \geqslant 20$ mm h^{-1} or local maximum $R \geqslant 4$ mm h^{-1}	Tao *et al.* (1989)
	A_{ps}	A_2	stratiform areas	$R \geqslant 0.5$ mm h^{-1}	
		A_3	trailing areas	$IP \geqslant 1$ kg m^{-2}	
Non-precipitating environment (A_{np})	A_{sh}	A_4	shallow clouds	$q_c + q_r + q_n + q_h$ $\geqslant 5.10^{-6}$ kg kg^{-1}	Sui *et al.* (1994)
	$A_{a.s}$	A_5	icy anvils	$q_c + q_r + q_n + q_h + q_i$ $\geqslant 5.10^{-6}$ kg kg^{-1} and no shallow clouds	
		A_6	clear-sky columns		

R is the surface precipitation and $IP = \int_0^H \rho(q_r + q_n + q_h)\mathrm{d}z$ is the vertically integrated precipitating hydrometeor content. A_T corresponds to the total domain so that; $A_T = A_p + A_{np} = \sum_{i=1}^{6} A_i$. We also define intermediate areas; $A_{pc} = A_1$, $A_{ps} = A_2 + A_3$, $A_{sh} = A_4$ and $A_{a.s} = A_5 + A_6$.

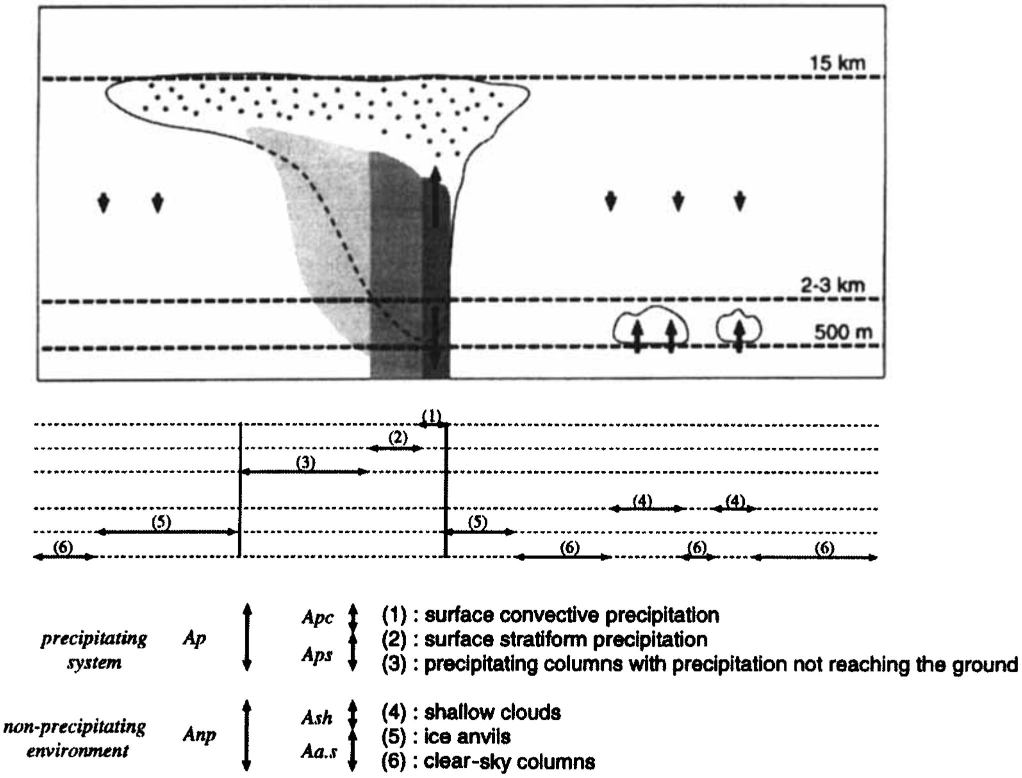

Figure 1. Schematic view of the cloud ensemble and its decomposition.

(*d*) *Budget equations*

Thermodynamic variables θ and q_v are horizontally averaged over internal areas A_i defined during the time interval $[t_1, t_2]$. The average of a quantity α over A_i is written:

$$\overline{\alpha}^i(z) = \frac{1}{\int_{t_1}^{t_2}\iint_{S_i}\mathrm{d}s\mathrm{d}t}\int_{t_1}^{t_2}\iint_{S_i}\alpha(z)\,\mathrm{d}s\mathrm{d}t \tag{3}$$

where S_i is the horizontal surface of the subdomain A_i at time t. For the particular case where the subdomain is defined as the whole simulation domain, the average is written as $\overline{\alpha}^\mathrm{T}$. The application of this operator results in the following budget equations expressed in terms of heat source and moisture sink:

$$\pi_0\overline{\frac{\partial\theta}{\partial t}}^i = -\frac{\pi_0}{\rho_0}\overline{\frac{\partial}{\partial x}\rho_0u\theta + \frac{\partial}{\partial y}\rho_0v\theta}^i - \frac{\pi_0}{\rho_0}\overline{\frac{\partial}{\partial z}\rho_0w\theta}^i + \pi_0\overline{D_\theta}^i + \overline{Q^*}^i + \overline{Q_\mathrm{R}}^i \tag{4}$$

$$-\frac{L_\mathrm{v}}{c_p}\overline{\frac{\partial q_\mathrm{v}}{\partial t}}^i = \frac{L_\mathrm{v}}{c_p\rho_0}\overline{\frac{\partial}{\partial x}\rho_0uq_\mathrm{v} + \frac{\partial}{\partial y}\rho_0vq_\mathrm{v}}^i + \frac{L_\mathrm{v}}{c_p\rho_0}\overline{\frac{\partial}{\partial z}\rho_0wq_\mathrm{v}}^i - \frac{L_\mathrm{v}}{c_p\rho_0}\overline{D_{q_\mathrm{v}}}^i + \overline{Q}^i \tag{5}$$

where the total transport has been split into horizontal and vertical terms (the first two terms on the right-hand side of Eqs. (4) and (5)). The contribution of each internal area A_i to the budget at the domain-scale A_T is proportional to its average occupation rate σ_i:

$$\sigma_i = \frac{\int_{t_1}^{t_2}\iint_{S_i}\mathrm{d}s\mathrm{d}t}{(t_2 - t_1)\,S_\mathrm{T}} \tag{6}$$

where S_T is the surface of the simulation domain. The budget equations at the whole domain-scale become:

$$\pi_0\overline{\frac{\partial\theta}{\partial t}}^\mathrm{T} = -\frac{\pi_0}{\rho_0}\overline{\frac{\partial}{\partial z}\rho_0w\theta}^\mathrm{T} + \overline{D_{Q_1}}^\mathrm{T} + \overline{Q^*}^\mathrm{T} + \overline{Q_\mathrm{R}}^\mathrm{T} \equiv Q_1 \tag{7}$$

$$-\frac{L_\mathrm{v}}{c_p}\overline{\frac{\partial q_\mathrm{v}}{\partial t}}^\mathrm{T} = \frac{L_\mathrm{v}}{c_p\rho_0}\overline{\frac{\partial}{\partial z}\rho_0wq_\mathrm{v}}^\mathrm{T} + \overline{D_{Q_2}}^\mathrm{T} + \overline{Q}^\mathrm{T} \equiv Q_2 \tag{8}$$

which correspond to the apparent heat source Q_1 and apparent moisture sink Q_2 at the A_T scale, as the large-scale forcings vanish for the present case-study. Horizontal fluxes vanish at the domain-scale due to the cyclic lateral-boundary conditions (see 3.1), and are commonly neglected in mass flux convection schemes.

3. THE SIMULATION

(*a*) *The case-study and conditions of simulation*

The case-study corresponds to lines of convection observed on the 17 February 1993 over the west equatorial Pacific, during the TOGA-COARE experiment. It is presented in Jabouille *et al.* (1996) and Jabouille (1996). Isolated lines were developing from clear-sky conditions during the second part of the night, with a life cycle of the order of a few hours. Their length reached 100–200 km in their mature stage and they were lying approximately parallel to the low-level shear.

The conditions of simulation are similar to Jabouille *et al.* (1996) except for the inclusion of ice-phase microphysics. The model is used with cyclic lateral-boundary conditions, and starts at 22 h (local time) from horizontally homogeneous profiles derived from

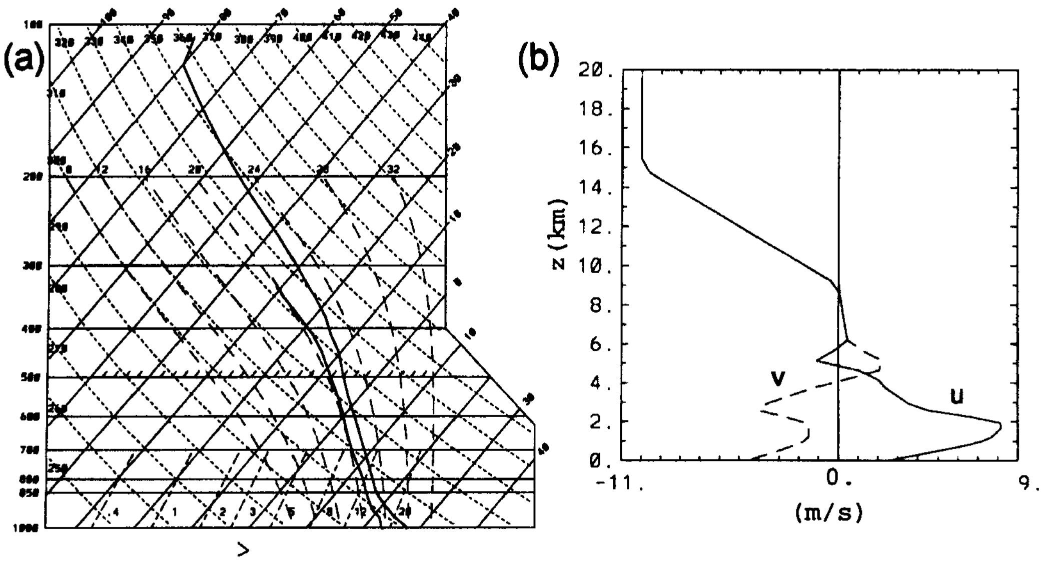

Figure 2. Initial vertical profiles: (a) skew-T log-P diagram, (b) wind components in m s^{-1}.

a radio-sonde sounding (Fig. 2). This is a typical sounding for a tropical oceanic atmosphere, with a moderate amount of convective available potential energy (970 J kg^{-1}), over a shallow boundary layer, about 600 m deep. It must be noted that no large-scale advection is introduced for this case. Thus, external forcing consists only of surface heat fluxes and radiation. The model develops convection by itself, starting from small random perturbations of temperature, thus avoiding an artificial initialization by a cold or warm perturbation which is often used.

The simulation is performed in 3D on a total domain of 90 by 90 km^2 in the horizontal and 20 km in height. The horizontal grid spacing is 900 m. The vertical grid is stretched, from 70 m resolution in the lower layers up to 700 m above 10 km. A time step of 10 s is used and the model integration proceeds over 10 hours of physical time.

(*b*) *Temporal evolution of global parameters*

The first hour and a half corresponds to a transition stage, STG0, allowing the building up of a dry boundary layer starting from homogeneous conditions. Then the system develops three distinct convective stages (Fig. 3).

Between $1\frac{1}{2}$ and $4\frac{1}{2}$ hours, STG1, small cumuli appear at the top of the boundary layer, but without generating precipitation. The horizontal resolution (900 m) is too crude to precisely simulate this shallow-convection stage. However, a higher resolution (300 m) simulation showed similar results and organization, but greater intensity (vertical velocities of up to 1 m s^{-1}).

Two distinct precipitation events then follow (Fig. 3(a)). The first one, STG2 between $4\frac{1}{2}$ and $7\frac{1}{2}$ hours, is due to numerous individual warm clouds, whose tops mainly stay below the height of the 0 °C isotherm (Fig. 3(c)). Nevertheless after $5\frac{1}{2}$ hours significant quantities of graupel are formed from the supercooled rain as cells rise to reach the 8 km level. The second precipitating event, STG3 between $7\frac{1}{2}$ and 10 hours, corresponds to deeper convection, with cloud tops reaching the tropopause (Fig. 3(c)). Solid hydrometeor contents then become higher (Fig. 3(b)). The graupel content is strongly coupled to precipitation

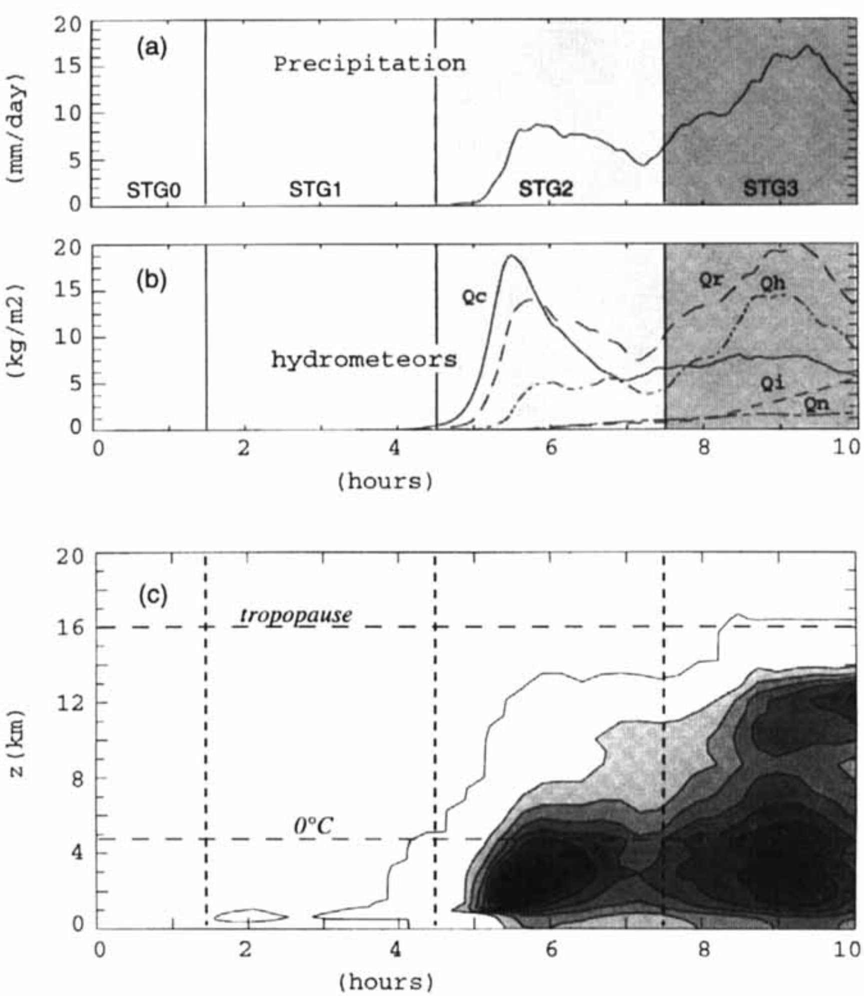

Figure 3. Time histories of (a) precipitation in mm day^{-1}, (b) domain integrated water contents for each hydrometeor species in kg m^{-3} and (c) vertical profile of the total hydrometeor field $q_c + q_r + q_i + q_n + q_h$ averaged at the domain-scale in kg kg^{-1}, the contour interval is 10^{-5}kg kg^{-1}. See text for further explanation.

and decreases between 9 and 10 hours. On the other hand, ice crystal content grows during the last two hours, simultaneously with the increase in extent of ice anvils.

Figure 4 shows a sequence of instantaneous surface precipitation rates taken every hour during STG2 and STG3. In order to better follow precipitation zones, the figures have been drawn in a framework moving eastward and southward at 5 m s^{-1} and 1 m s^{-1}, respectively. First precipitation appears around 5 hours (Fig. 4(a)) falling from a group of cells aligned in the E–W direction. This structure dominates throughout STG2, but numerous isolated cells appear around $5\frac{1}{2}$ hours elsewhere in the simulation domain (Fig. 4(b) at 6 hours). After 7 hours individual cells tend to form bigger structures with a length of a few tens of km, aligned approximatively WSW–ENE, with less intense precipitation areas extending along WNW–ESE. The propagation speed of these systems also increases to reach about double the moving-framework speed.

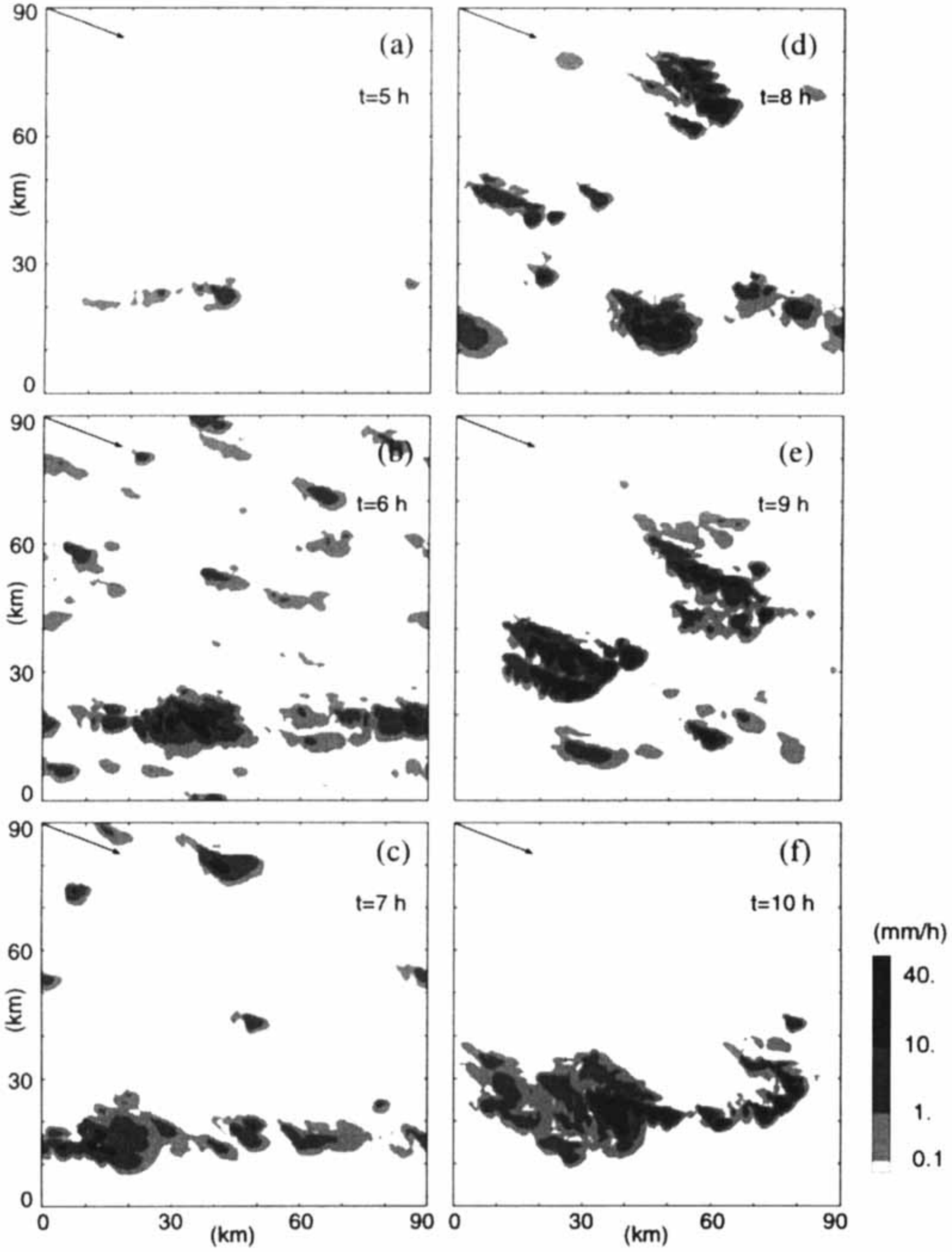

Figure 4. Instantaneous fields of surface precipitation at t = 5 h, 6 h, 7 h, 8 h, 9 h, and 10 h. The arrow shows the horizontal displacement of the area (relative to the surface) in one hour (i.e. between two consecutive pictures), due to a translation of 5 m s^{-1} from west to east and 2 m s^{-1} from north to south.

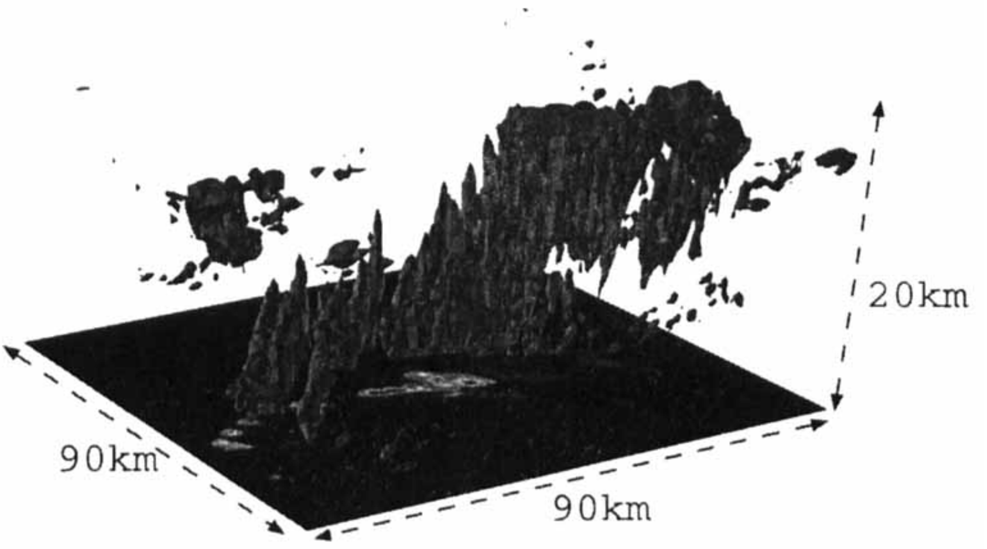

Figure 5. Three dimensional view at 10 h taken from the north-east of the instantaneous field of simulated clouds (isosurfaces 0.32 g kg^{-1}) of the sum of hydrometeors present, with associated surface precipitation.

A simulation performed over a domain four times larger exhibits similar structures, and available radar observations also show individual convective entities on the same scale as modelled, without extended stratiform parts (Jabouille 1996).

An instantaneous 3D view (Fig. 5) illustrates the simulated convective system during STG3, formed of an ensemble of different cloud types at different stages of their life cycle. Shallow clouds, deep growing cells as well as ice anvils are present simultaneously.

(c) *Temporal evolution of the cloud system impact*

The temporal evolution of the budgets (Figs. 6 and 7) allows us to better describe the cloud ensemble behaviour in terms of the large-scale impact. STG1 has a weak impact on heat, whereas the moisture transport by planetary boundary-layer (PBL) eddies and cumuli is very efficient (up to about 20 deg C d^{-1}) at drying the first 300 m and moistening the 300–1300 m layer (Figs. 6(e) and 7(d)). This large storage of moisture in the PBL during this pre-deep-convection stage is obviously related to the oceanic nature of this case-study with about 130 W m^{-2} and 15 W m^{-2} surface latent- and sensible-heat fluxes, respectively.

STG2 appears explosive (Fig. 6(d)) and allows the sudden release of latent heat stored during STG1. Clouds are very efficient at vertically redistributing heat and especially moisture, resulting in significant drying below 1300 m and moistening (Fig. 7(e)) from 1300 m up to 5 km. The intense character of this convective stage is associated with the simultaneous development of many clouds (Fig. 4(b)), in an environment that has previously been strongly destabilized and moistened during STG1. This stage has been recovered with the same characteristics by all sensitivity simulations performed to test the impact of the resolution, the domain size and microphysics parameters. Jabouille (1996) found that the growth rate of the medium-cloud and high-cloud cover estimated from satellite pictures was large, although a little less intense than simulated. This peak in the density of modelled clouds is probably enhanced due to a lack of spatial inhomogeneities in such idealized simulations. It may be less intense in reality, as natural variability is expected to trigger deep convection sooner in certain places.

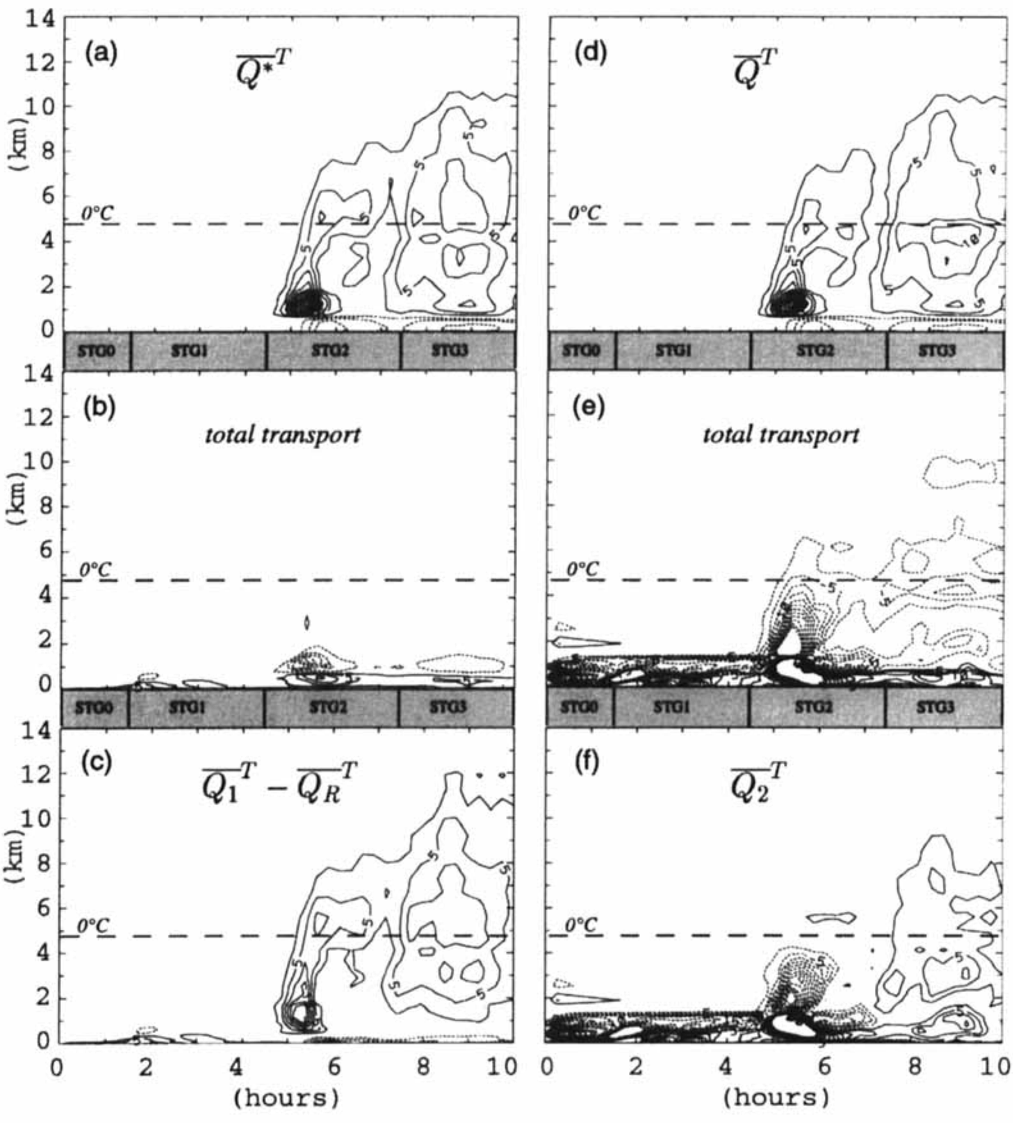

Figure 6. Time evolution averaged at the domain scale A_T, of the heat source budget: (a) total latent-heat release, Q^*, (b) convective transport and (c) convective apparent heat source, $Q_1 - Q_R$; and of the moisture sink budget: (d) latent-heat release, Q, (e) convective transport and (f) apparent moisture sink, Q_2. The time averaging period is $\frac{1}{4}h$, and the contour interval is 5 K day^{-1}. The figures are limited in the vertical to the cloud system depth (14 km). See text for further explanation.

Finally, STG3 presents more similarities with previous analyses of deep convective systems such as a squall line; these include the importance of humidity transport and the impact of fusion processes around 5 km altitude as quantified by the difference between Q^* and Q (not shown). This stage allows the transfer of water vapour throughout the full depth of the troposphere.

In short, the above analysis stresses that the temporal evolution of the simulated-cloud ensemble is made up of a succession of distinct stages. In particular, deep convection

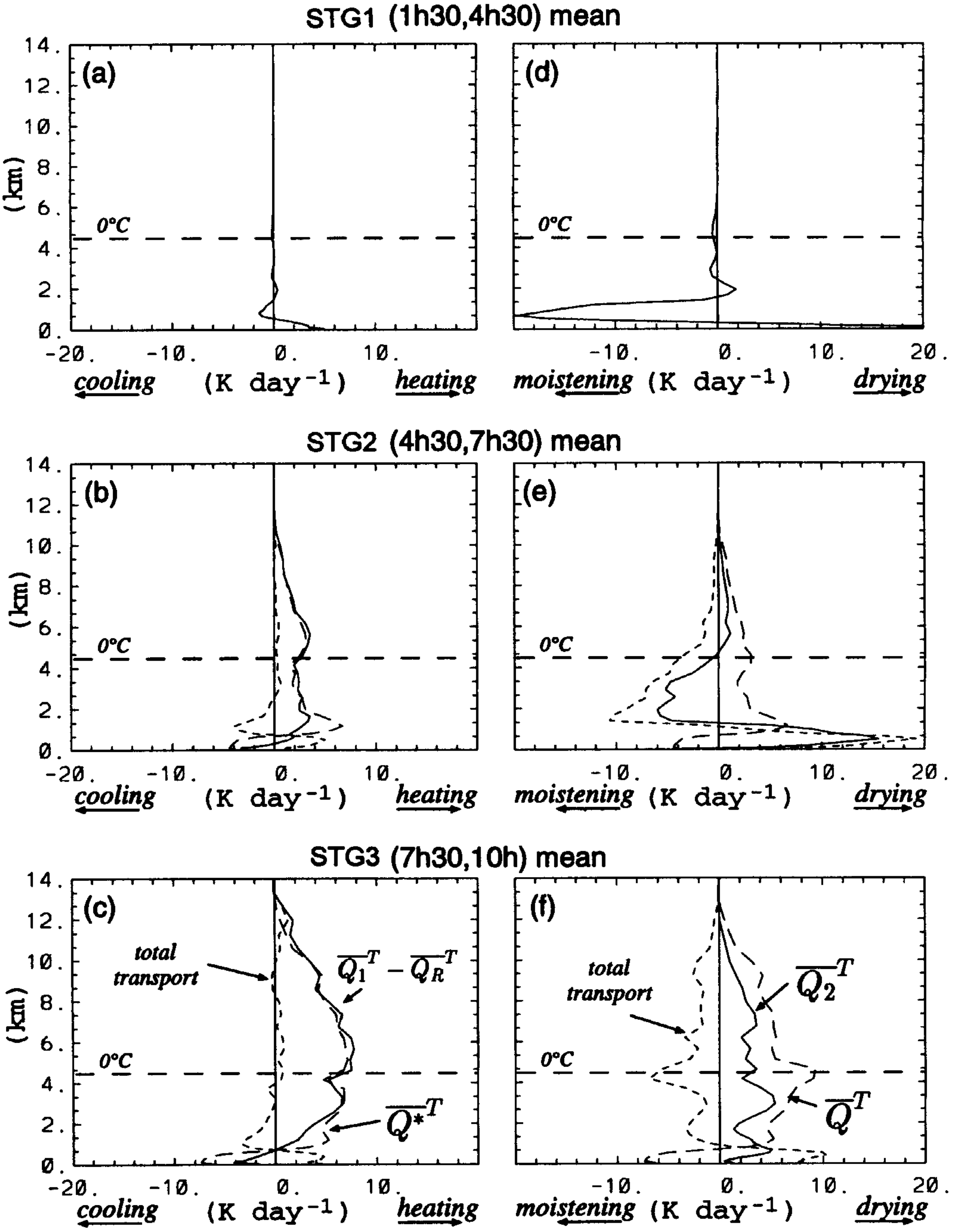

Figure 7. Vertical profiles of the heat and moisture budgets, averaged at the domain-scale A_T during the three stages STG1, STG2 and STG3 of the simulated cloud system. See text for further explanation.

occurs after shallower convective stages have moistened sub-layers and introduced more horizontal variability.

In the following analysis (except in 4(a)), we focus on the last deep convective event.

4. DESCRIPTION OF INTERNAL AREAS

The simulated atmospheric volume appears as a composite domain, including areas of greatly differing properties, such as deep convective cells or clear-sky columns. Very strong latent-heat releases occur in the former, whereas radiative cooling is the only diabatic source in the latter. In this section we attempt to give a dynamical and thermodynamical description of the different internal zones making up the total domain, as defined in section 2(c).

(*a*) *Area occupancy*

In terms of area occupancy (Fig. 8) shallow clouds first appear at the end of the fourth hour, and quickly develop over more than 50% of the total domain during STG2, as opposed to STG3. The surface convective precipitation area is always very restricted, covering about 4% of the total domain, a value of the same order as found by Tao *et al.* (1987). The precipitating system A_p occupies a larger area ($\approx$ 20%), whereas shallow clouds are still numerous during the deep-precipitation stage ($\approx$ 25%). Icy anvil cover grows from 0% to about 30% during the last two hours of simulation. At this time-scale anvil evolution seems uncorrelated with convective activity once they have been generated. Throughout the simulation clear sky represents an important fraction of the domain (41% on average for STG3). Thus, it appears that areas of active convection cover a very small fraction of the domain, so that all other parts will provide an important contribution to the total budget of the system.

(*b*) *Vertical velocities and mass fluxes*

Figures 9(a) and (b) show the profiles of mean vertical velocity in the different internal areas. In the convective precipitation area A_{p_c}, the profile is typical of one of the convective parts, with subsidence (-25 cm s^{-1}) at low levels (under 1500 m) and ascent above

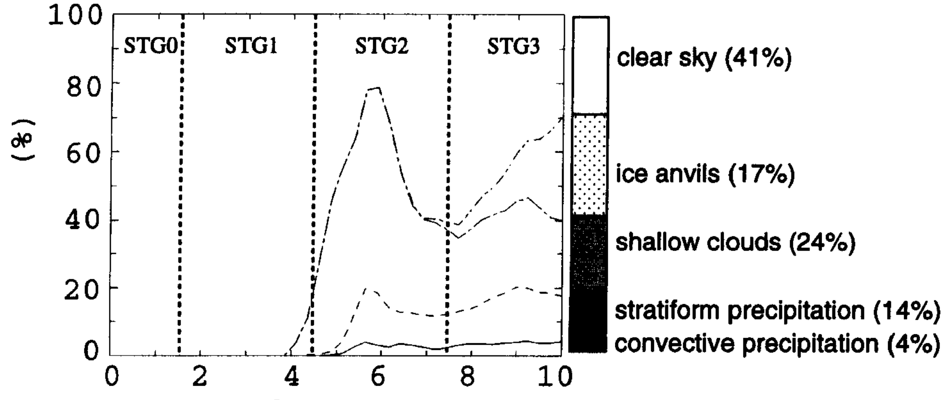

Figure 8. Time history from 0 h to 10 h of area occupancy for: convective precipitation A_{pc} (solid line), the precipitating system A_p (dashed lines), A_p plus shallow-cloud area A_{sh} (dashed-dotted line), A_p plus A_{sh} plus anvil clouds (dashed-dotted-dotted line). Numbers in brackets are the average area occupancies from 8 h to 10 h. See text for further explanation.

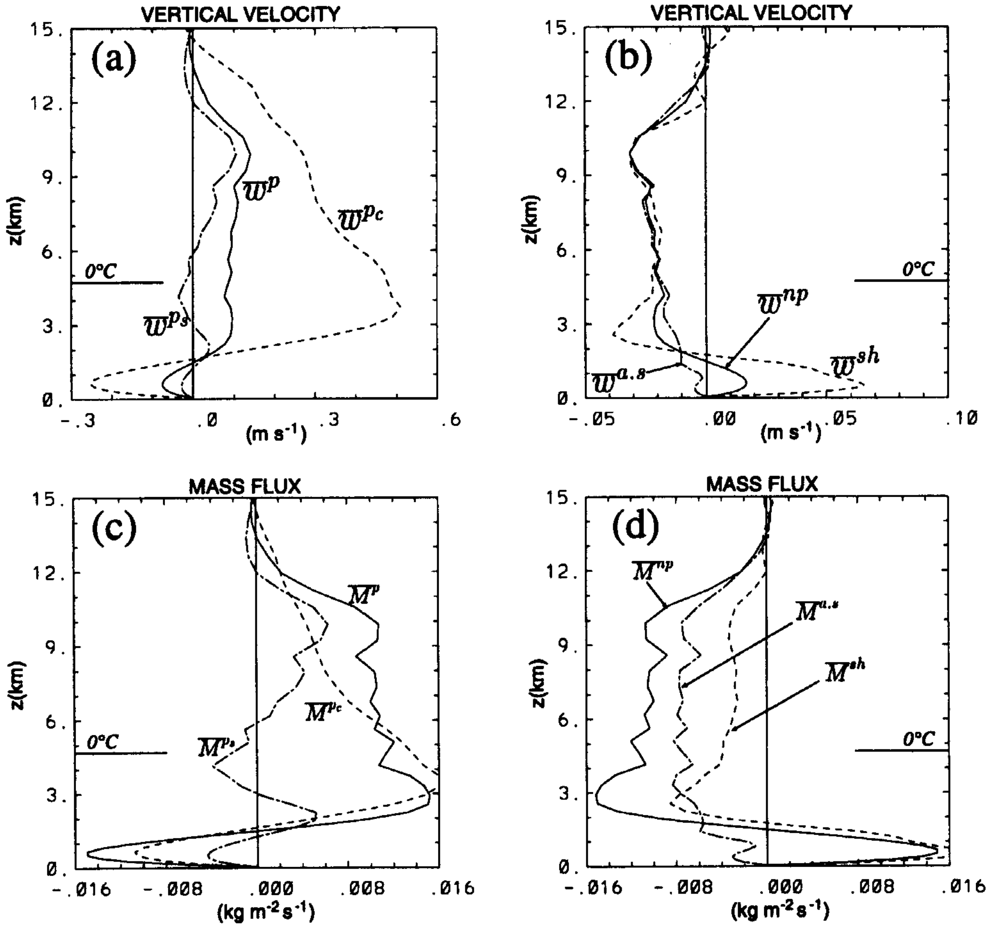

Figure 9. Vertical profiles of vertical velocity averaged from 8 h to 10 h for: (a) the precipitating system (A_p), its convective (A_{pc}) and stratiform (A_{ps}) parts and (b) the non-precipitating environment (A_{np}), the shallow clouds area included in it (A_{sh}) and the remaining anvil plus clear-sky columns ($A_{a.s}$). (c) and (d) are the same as (a) and (b) but for vertical mass fluxes. See text for further explanation.

(maximum of 50 cm s^{-1} at about 3 km). These values of draught extrema are moderate and agree with both aircraft data (Lucas *et al.* 1994; Jorgensen and LeMone 1989) and previous numerical studies (Tao *et al.* 1987) for the case of tropical oceanic convection.

Due to the stratiform area A_{p_s}, the mean vertical velocity of the total precipitating system A_p is weaker and its maximum is located higher. It must be noticed that the profile of $\overline{w}^{p_s}$ is different from the known classical profile of vertical velocity in stratiform parts of organized long-living squall lines (Gamache and Houze 1982; Tao and Simpson 1989). Instead of two separate layers, the lower subsiding and the higher ascending, the present profile shows 4 distincts layers, and 2 local maxima. The less intense precipitation area A_{p_s} includes both a high and a low layer of cloud activity. Thus, the stratiform part of the precipitating system appears as the superposition of low-level developing cells and high-level clouds, located in the vicinity of convective precipitating areas.

Above 2 km the non-precipitating environment A_{np} is subsiding on average (Fig. 9(b)), with similar values (-2 to -3 cm s^{-1}) for all non-precipitating internal areas above the shallow cloud layer. The icy-anvils region appears dynamically active (Fig. 10), with ascent

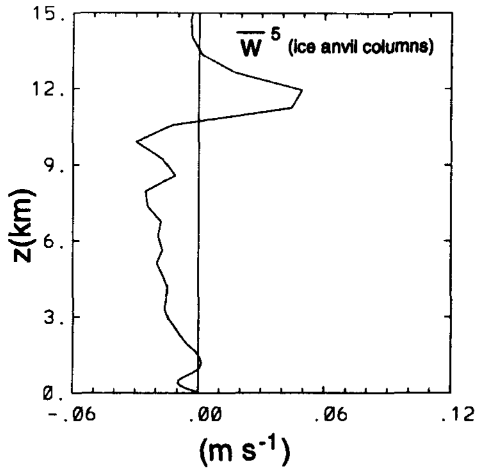

Figure 10. Vertical profile of vertical velocity, w, in the area of ice-anvil clouds A_5, averaged over 8h–10 h (w is negative below the anvil).

(up to 5 cm s^{-1}) in the 10.5–13 km layer, explaining its persistent character. Below 2 km the area of shallow convection is the only ascending zone (6 cm s^{-1}) of the domain. This suggests that the shallow convection during STG3 is forced by a mean ascent compensating the subsiding motion prevailing below the precipitating part A_p of the cloud system.

The total mass fluxes per area (Figs. 9(c) and (d)) quantify the vertical transports inside the domain. Furthermore, cloud mass flux is a crucial quantity for mass flux convection schemes. Firstly, the mass flux in A_p results mostly from the vertical motion in A_{p_c}. The contribution of A_{p_s} is significant at higher layers where it takes over from the mass flux in A_{p_c}. Nevertheless, it remains of the same order as the mass flux in A_{p_c}, indicating that the less intense precipitating area, A_{p_s}, is not very active.

On a larger scale it is noticeable that mass transfers between A_p and A_{np} are mainly concentrated below 3 km and above 10 km, with only few net exchanges between these two altitudes. These two parts thus evolve as two separated columns, as the vertical flux of mass stays almost constant in the 3–10 km layer.

(c) *Latent-heat release*

The latent-heat release, $\overline{Q^*}^T$ (Fig. 11(a)), is responsible for a heating of the troposphere above 1 km up to 12 km, reaching a maximum value of 7 K d^{-1}. Its profile exhibits some classical features, such as strong cooling below 1 km caused by raindrop evaporation (Lafore *et al.* 1988), and a local minimum below the height of the 0 °C isotherm associated with solid hydrometeor melting (Caniaux *et al.* 1994).

The major contribution to $\overline{Q^*}^T$ comes from the A_p, first from the convective area A_{p_c}, but also from the weaker precipitating zones A_{p_s} at higher and lower levels (Fig. 11(b)). Nevertheless, as already found by Gregory and Miller (1989) latent heat released by shallow clouds (the A_{np} curve in Fig. 11(a)) cannot be neglected. These clouds are responsible for intense condensation heating in a 1 km deep layer, and for large cooling by cloud droplet evaporation above.

A comparison of vertical mass fluxes (Fig. 9(c)) and latent-heat release (Fig. 11(b)) for the different internal areas shows a strong correlation between these two fields. As previously found for mass fluxes, the convective precipitating area (covering a few % of

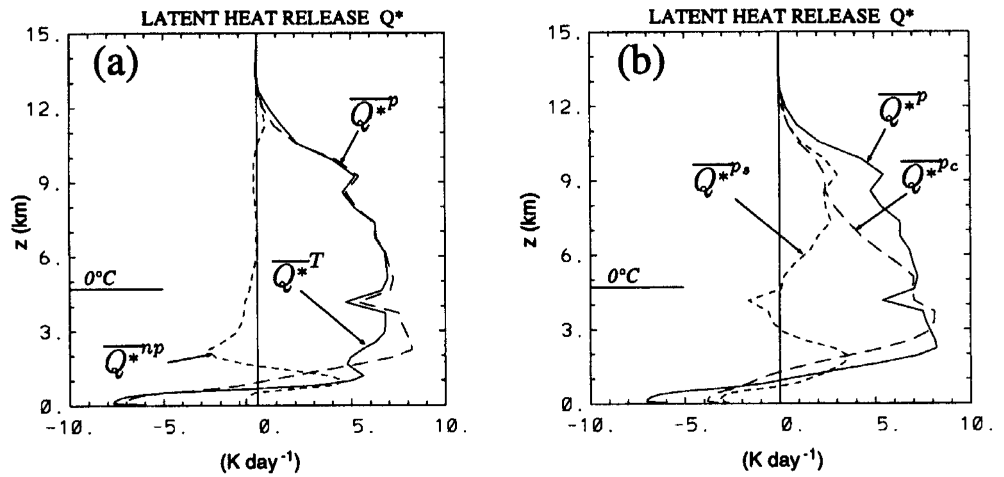

Figure 11. Vertical profiles of latent-heat release for different areas ($\sigma_i \overline{Q^*}^i$) over 8 h to 10 h (a) for the total domain (A_T), the precipitating system (A_p) plus the non-precipitating environment (A_{np}), (b) same as (a) for A_p, its convective (A_{pc}) plus its stratiform (A_{ps}) parts.

the domain) is responsible for the major part of the latent-heat release occuring in A_p (Fig. 11(b)).

(*d*) *Temperature and water vapour deviations*

As shown by vertical-velocity and latent-heat release profiles, the total domain is composed of areas characterized by very different dynamical and thermodynamical behaviours. Nevertheless, temperature deviations (Figs. 12(a) and (b)) between these areas are extremely small, except at low levels where convectively generated cold pools are more than 1 K colder than the environment (Fig. 12(a)). Above 1 km A_{p_c} is the warmest, but potential temperature is only about 0.2 K warmer than the domain average, whereas the latent-heat release is of the order of 100 K day^{-1}. Averaging over shorter time periods (5 minutes) does not lead to temperature deviations higher than 0.4 K. Existing aircraft data from convective cores of tropical oceanic convective systems also stress the very low temperature excess (Lucas *et al.* 1994; Jorgensen and LeMone 1989). A direct comparison with our results is not possible because different criteria have been used, nevertheless these two distinct approaches lead to convergent results: i.e. temperature excesses in convective cells are significantly smaller than would be expected from an undiluted air parcel lifted from the boundary layer. Previous numerical studies (Tao *et al.* 1987; Soong and Tao 1980) also found small temperature deviations, although they explain their results by a large temporal averaging period (Soong and Tao 1980).

Above 1 km A_{p_s} is not significantly warmer than the domain average (Fig. 12(a)). The height of the 0 °C isotherm can be seen in this area (around 4.7 km). It is more pronounced than in the convective precipitating area where warm-phase microphysical processes are dominant. In the environment of A_p, temperature deviations become extremely small (Fig. 12(b)). This validates a common approximation used by parametrization schemes.

Unlike deviations of temperature, water vapour deviations δq_v (Figs. 12(c) and (d)) are not weak and are closely related to vertical velocities (Fig. 9). In-cloud air is moister than air in cloud-free areas, deviations of specific humidity δq_v reaching 0.6 g kg^{-1} in A_{p_c}.

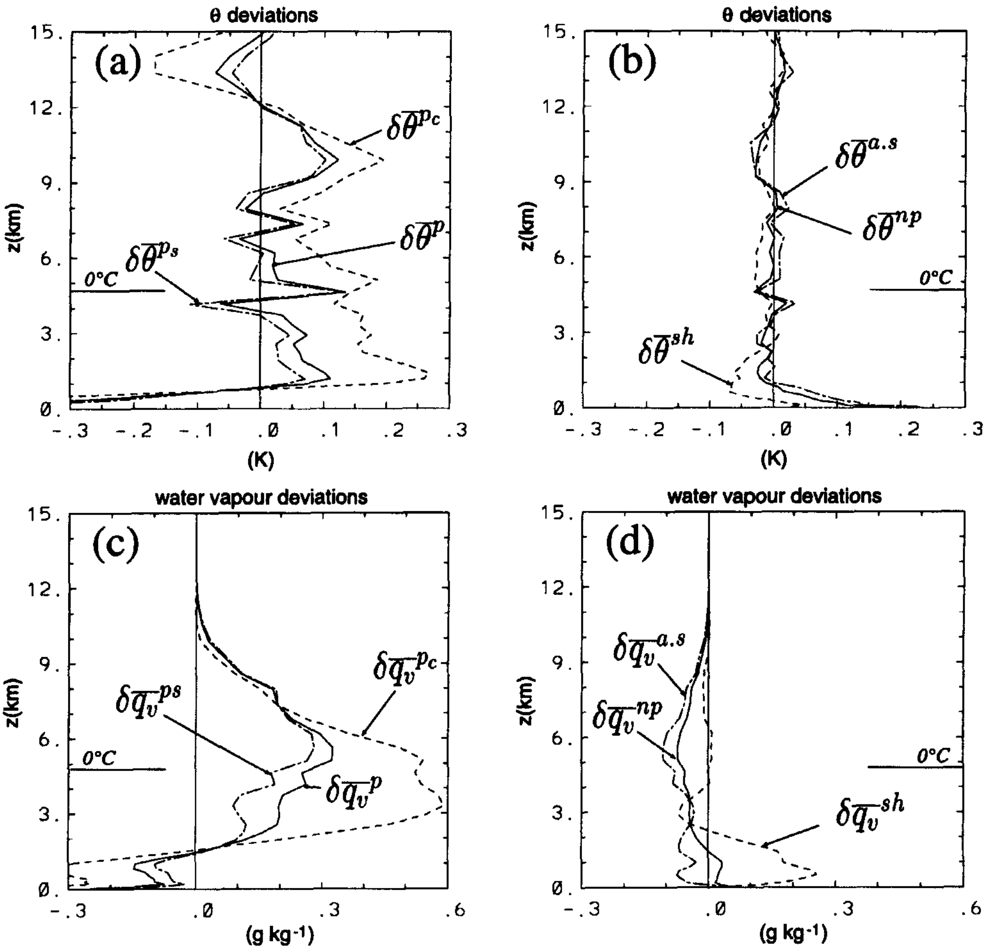

Figure 12. (a) and (b): same as Fig. 9 (a) and (b) but for deviations of potential temperature; (c) and (d): same as (a) and (b) but for deviations of water vapour q_v - $\overline{\delta\alpha}^k = \overline{\alpha}^k - \overline{\alpha}^T$.

(e) *An equilibrium of density*

Though the deviations of the potential temperature θ give a first estimate of buoyancy, it is given more accurately by deviations of the virtual liquid and solid potential temperature (i.e. virtual potential temperature including the water loading) θ_{vl}, defined by: $\theta_{vl} = \theta\left(1 + \epsilon q_v - \sum q_\gamma\right)$, with $\sum q_\gamma$ the sum of the hydrometeor-specific mixing ratios. Water vapour and hydrometeors act in opposite ways. Excess water vapour in precipitating areas increases buoyancy in these areas, whereas hydrometeor loading decreases it. The resulting $\delta\theta_{vl}$ (Fig. 13) are still weaker than the corresponding $\delta\theta$ (Fig. 12(a)). It appears that the system exhibits an *equilibrium of density*, resulting firstly from very small temperature deviations, and further reinforced by the net effect of water in all of its phases. The impact of water loading in reducing buoyancy, and thus vertical velocity, is once again clear from the present simulation, in agreement with the analysis of observations (e.g. Xu and Emanuel 1989).

Buoyancy excesses that are necessary to generate convective clouds must therefore occur in very small and localized areas and on short time-scales. This *equilibrium* shows

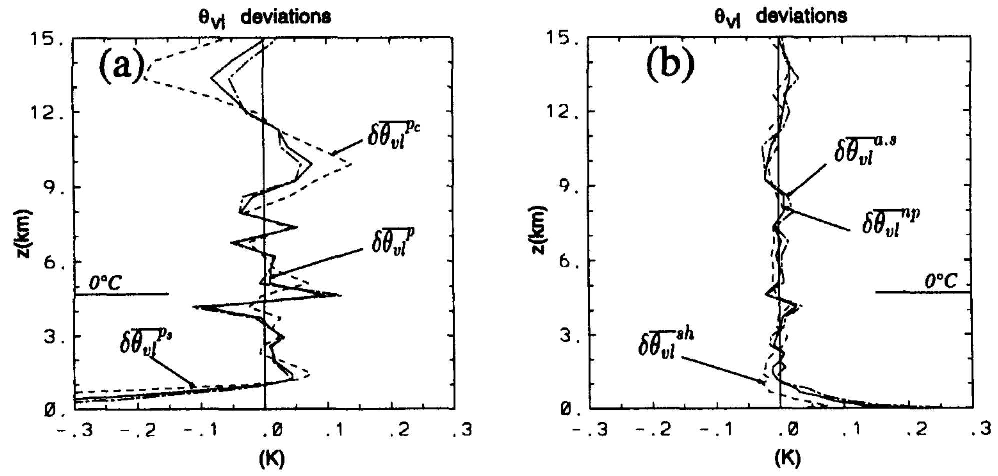

Figure 13. (a) and (b): same as Fig. 11 (a) and (b) but for deviations of $\delta\theta_{\mathrm{vl}}$.

the speed and efficiency of the convection in modifying the environment, through compensating subsidence and adjustment by internal gravity waves. In practice, an important consequence is that we obtain a relationship between thermodynamics and microphysics inside and outside of clouds, that could be useful for a convection scheme.

Some convection mass flux schemes using a bulk-cloud model (as opposed to a cloud spectrum) already try to limit temperature excess in clouds (Gregory and Rowntree 1990). However, if the relation θ_{vl} (cloud) $= \theta_{\mathrm{vl}}$ (clear sky) was abruptly applied to an existing scheme it is possible that it could lead to excessive hydrometeor contents, due to the in-cloud temperature used in the scheme being higher.

5. THERMODYNAMICAL BUDGETS

(*a*) *A sum of different processes*

In the present case, without any large-scale advection, the budget equations of heat source and moisture for the whole domain (Eqs. 7 and 8) correspond directly to the apparent heat source Q_1 and apparent moisture sink Q_2. Above the lowest kilometre, the system heats and dries during STG3, but profiles of Q_1 and Q_2 are quite distinct (Figs. 14(a) and (b)). This is now a classical feature that has often been highlighted for many convective systems, both from observations (Yanai *et al.* 1973; Johnson 1984) and modelling studies (Tao and Soong 1986; Lafore *et al.* 1988; Gregory and Miller 1989; Caniaux *et al.* 1994).

Q_1 shows a maximum heating of about 6 K day^{-1} located around 5–6 km, in agreement with profiles of Lin and Johnson (1996) over the TOGA-COARE region. The heating is mainly due to the latent-heat release $\overline{Q^*}^{\mathrm{T}}$. The sharp minimum at 4 km corresponds to melting occurring below the height of the 0 °C isotherm. Convective transports are significant mainly below 2 km, where they tend to reduce the subcloud evaporation of precipitating droplets and the net condensation between 1 and 2 km. Radiative effects are approximately constant up to 9 km, of the order of 1 K day^{-1}. We can see the radiative impact of high-level anvil clouds, with a cloud top cooling at around 12–13 km and a cloud base warming at 11 km.

The profile of Q_2 is more complex, it shows several minima and maxima. In particular, we can see two maxima of Q_2 at around 3–4 km and 7 km. Nevertheless there is also a maximum located above the top of the subcloud layer ($\sim$ 1 km).

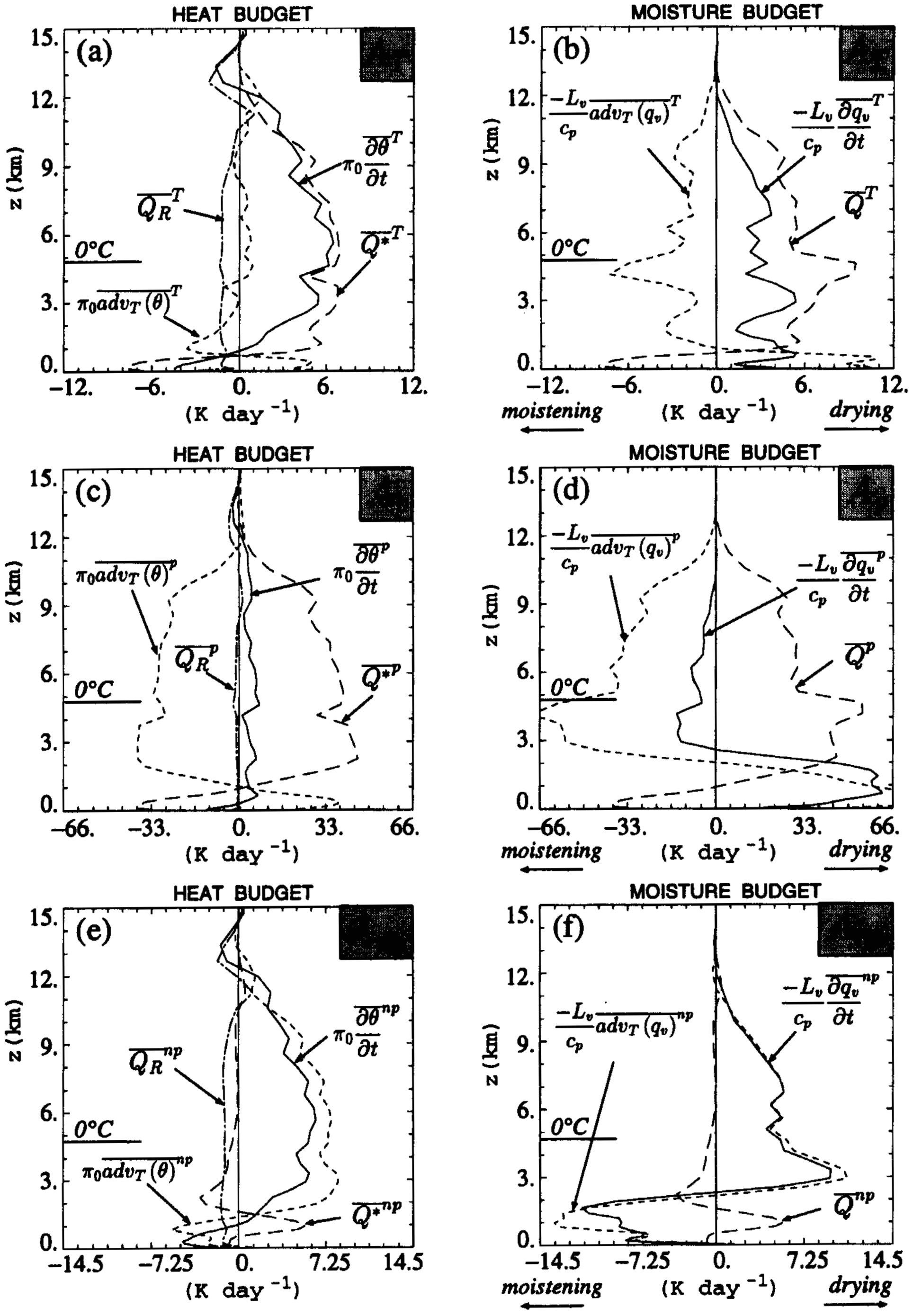

Figure 14. Budgets of (a) heat and (b) moisture horizontally averaged over the whole domain A_T and from 8 h to 10 h; (c) and (d) same as (a) and (b) but for the precipitating area A_p; (e) and (f) same as (a) and (b) but for the non-precipitating area A_{np}. The horizontal scale is such that, multiplied by the rate of occupation (σ_p or σ_{np}) of the considered area, it gives the contribution of each area to the total budgets over A_T with the same horizontal scale.

In the present case, as found by previous modelling studies (Lafore *et al.* 1988; Caniaux *et al.* 1994), differences between Q_1 and Q_2 profiles result in the main from differences in convective vertical transports of heat and moisture. In effect, convective transports of moisture are not negligible for any layer, being of the same order as the sink of moisture due to microphysical processes $\overline{Q}^{\mathrm{T}}$. Convective transports act in opposition to $\overline{Q}^{\mathrm{T}}$, redistributing water vapour from the low layers up to the free troposphere. Several local minima appear on the vertical profile, corresponding to maxima of moistening. The lowest one, at 2 km, explains the local minimum drying of Q_2 at this altitude. Another, just below the height of the 0 °C isotherm, counteracts the local maximum of $\overline{Q}^{\mathrm{T}}$. Caniaux *et al.* (1994) found similar behaviour for the case of a squall line. The maximum of $\overline{Q}^{\mathrm{T}}$ can be explained by the cooling due to melting, which is responsible for a decrease of water vapour mixing ratio at saturation.

(*b*) *A sum of contributions from internal areas*

In this section previous budgets (Figs. 14(a) and (b)) are split into the sum of budgets over the precipitating area A_{p} (Figs. 14(c) and (d)) and the non-precipitating environment A_{np} (Figs. 14(e) and (f)) on the basis of the partitioning equations (4) and (5). The relative contribution of each internal area is proportional to its average area occupancy, $\sigma_{\mathrm{p}} = 18\%$ and $\sigma_{\mathrm{np}} = 82\%$ respectively. It allows us to analyse where, and through which mechanisms, temperature and water vapour modifications occur.

As already noted, most of the latent-heat release Q^* occurs in A_{p} (Fig. 14(c)). However, the contribution of this part of the domain to the total heating is weak. In fact most of the resulting heating occurs in the environment A_{np} (Fig. 14(e)). This is because in A_{p} transports approximately balance $\overline{Q^*}^{\mathrm{p}}$, whereas they are responsible for the major part of the net heating in A_{np}, radiative heating accounting for only about 1 K day^{-1}. Thus, to first order, the domain-average temporal evolution of temperature can be explained by transports occurring in the environment. Simultaneously the precipitating system is approximately in equilibrium, as is assumed by some convection schemes (Arakawa and Schubert 1974; Tiedtke 1989).

Moisture budgets are more complex to analyse (Figs. 14(d) and (f)). In the precipitating area (Fig. 14(d)), above 3 km, $\overline{Q}^{\mathrm{p}}$ and transport approximately balance, resulting in a net moistening. Below 3 km a strong drying can be found, associated with transports in downdraughts. In the environment transports are the major processes and explain drying above 3 km as well as strong moistening below. Finally, below 3 km the net domain drying appears as the result of stronger drying in A_{p} than moistening in A_{np}. Above 3 km the opposite is found, as drying in the environment A_{np} dominates over moistening in A_{p}.

The above partitioning of budgets stresses the importance of transport by convective eddies. The next section furthers the analysis by separating vertical and horizontal transports.

(*c*) *Vertical transport and horizontal exchanges*

(i) *Decomposition of the total transport.* Total transport of a quantity α (here θ or q_{v}) in the internal area A_i is expressed as follows:

$$\overline{adv_{\mathrm{T}}\,(\alpha)}^{i} = -\overline{u\frac{\partial\alpha}{\partial x}}^{i} - \overline{v\frac{\partial\alpha}{\partial y}}^{i} - \overline{w\frac{\partial\alpha}{\partial z}}^{i} + \overline{D_\alpha}^{i}. \tag{9}$$

The first two terms on the right-hand side of this equation correspond to the horizontal advection:

$$\overline{adv_{\mathrm{H}}(\alpha)}^{i} = -\overline{u\frac{\partial \alpha}{\partial x}}^{i} - \overline{v\frac{\partial \alpha}{\partial y}}^{i}, \tag{10}$$

and the third one to the vertical advection. The last term $\overline{D_\alpha}^{i}$ is due to the subgrid-scale turbulence. As the contribution of turbulence to the transport comes mainly from the vertical component, it has been added to the vertical transport in the computation of diagnostics, so the vertical transport is defined as:

$$\overline{adv_{\mathrm{V}}(\alpha)}^{i} = -\overline{w\frac{\partial \alpha}{\partial z}}^{i} + \overline{D_\alpha}^{i}. \tag{11}$$

(ii) *Relative importance of horizontal and vertical advection.* In order to better understand heat and moisture exchanges by internal motions, transport is split into horizontal and vertical advection for the whole domain, A_{p} and A_{np} (Fig. 15).

Heat transport occurs mainly through vertical advection in A_{p} as in A_{np} (Figs. 15(c) and (e)). Thus the apparent heat source $\overline{Q_1}^{\mathrm{T}}$ (Fig. 14(a)) is explained at first order by the compensating subsidence occuring in A_{np}, as found by Gregory and Miller (1989). Horizontal exchanges tend to heat the precipitating system (Fig. 15(c)). On the other hand, in the non-precipitating environment horizontal exchanges with the precipitating environment are responsible for a weak cooling between 2 and 8 km (Fig. 15(e)). At the domain-scale, horizontal and vertical advection tend to compensate (Fig. 15(a)) and they both become difficult to analyse. Total vertical advection is a residual of vertical advection in the two parts of the domain, and horizontal advection is a complex combination of internal horizontal exchanges.

For moisture (Figs. 15(d) and (f)) above 3 km vertical advection is also the dominant term in comparison with horizontal advection. It brings moister air upwards in the precipitating system (Fig. 15(d)) and dries A_{np} through compensating subsidence (Fig. 15(f)). Below 3 km both horizontal and vertical exchanges become important for determining total transport. This is partly related to shallow-cloud activity in the non-precipitating environment.

A comparison of Figs. 15(d) and 14(d), enables us to show that vertical advection of moisture compensates $\overline{Q}^{\mathrm{p}}$ in the precipitating system. This simply corresponds to the fact that, in cloud areas where saturated conditions prevail, the increase of moisture by lifting is eliminated by condensation since no super-saturation is allowed. This balance is verified to a high degree of accuracy. It follows that the water evolution is explained by horizontal advection, as confirmed by a comparison of Figs. 15(d) and 14(d).

In the environment above 3 km horizontal exchanges tend to moisten A_{np} but remain small (Fig. 15(f)). At the domain-scale, as for heat budgets, these terms become very complex to understand (Fig. 15(b)). For moisture they are no longer systematically in opposition. Although both of them are necessary to enable retrieval of the total transport, horizontal advection is responsible for the mean moistening in the 2–8 km layer, which allows us to explain the decoupling between the Q and Q_2 profiles (Fig. 14(b)). This importance of horizontal moisture advection is consistent with the deviations of δq_{v} between the internal areas found in section 4(d). Moisture excesses are generated by convection, which then increases the humidity at the domain-scale by horizontal expansion, as illustrated by the rapid horizontal spreading of anvils seen on IR satellite imagery.

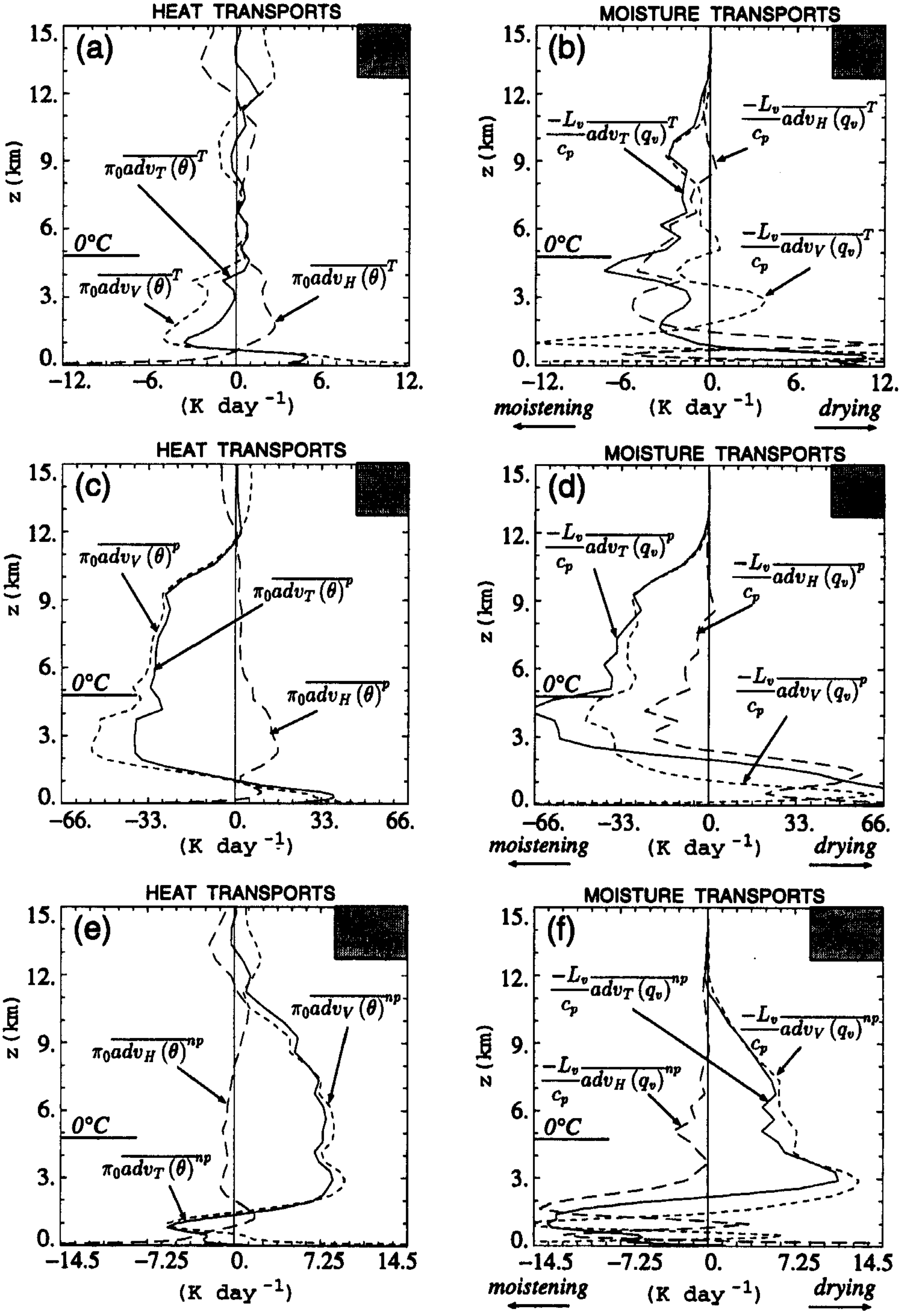

Figure 15. Same as Fig. 14 but for total transports, and their decomposition into horizontal and vertical advections, with similar horizontal scales.

6. CONVECTIVE TRANSPORTS

In this section we focus on the estimation of the impact of convective transports at the cloud-system-scale. As shown by previous budgets, this process is not very important for temperature but is crucial for water vapour, so it is necessary that a parametrization should estimate it correctly, especially for climate-change studies (Lindzen 1990).

Here we are concerned with the following question: *at what scale does convective transport occur?* In practice we define different internal areas, and determine whether the total convective transport is, or is not, well estimated by the sum of mean transports occuring in them. Vertical fluxes rather than divergence of vertical fluxes are analysed, as they lead to a more lucid explanation.

(*a*) *Total heat and moisture fluxes*

Vertical profiles of total heat and moisture vertical fluxes $c_p \pi_0 \rho_0 \overline{w\theta}^{\mathrm{T}}$ and $L_v \rho_0 \overline{wq_v}^{\mathrm{T}}$ are shown in Fig. 16 (solid lines). The structure of the heat flux (Fig. 16(a)) shows many similarities with those simulated and observed by Sommeria (1976) and Sommeria and LeMone (1978)—hereafter SL78—for shallow trade wind clouds. Firstly, the flux decreases linearly from the ocean surface (17 W m^{-2}) to the top of the mixed layer at 800 m. The minimum value (-18 W m^{-2}) greatly increases to more than -5 W m^{-2} when considering fluxes of virtual potential temperature. Above 800 m the flux increases to 25 W m^{-2} at 4 km, and decreases above that, except at 10 km where a second local maximum is present, related to high-level cloud activity. This signature is similar to the one obtained by SL78, except that here the upward flux concerns all the deep-convection layer up to 12 km, whereas flux stopped at 1400 m for the shallow-clouds layer of SL78.

Values of moisture flux at the surface and its vertical fluctuations are much more intense than those for heat (Fig. 16(b)). It increases from 130 W m^{-2} at the surface up to 215 W m^{-2} at 1 km, bringing water vapour from this layer up to the free troposphere where the flux gradually decreases. Above 12 km the flux becomes negligible. For convective stage STG3 considered here, it clearly appears that moisture previously stored below

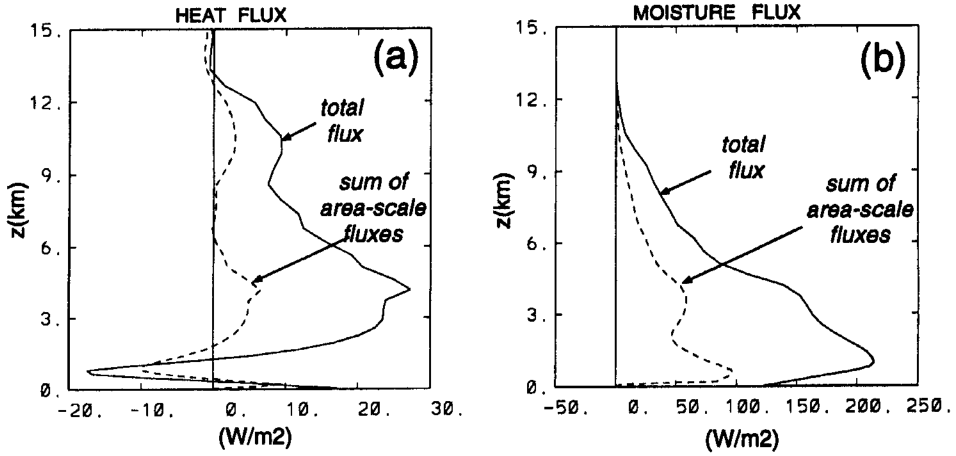

Figure 16. (a) Heat and (b) moisture fluxes. Total fluxes $c_p \pi_0 \rho_0 \overline{w\theta}^{\mathrm{T}}$ and $L_v \rho_0 \overline{wq_v}^{\mathrm{T}}$ (solid lines), and contributions of area-scale fluxes $c_p \pi_0 \rho_0 \sum_i \sigma_i \overline{w}^i \overline{\theta}^i$ and $L_v \rho_0 \sum_i \sigma_i \overline{w}^i \overline{q_v}^i$ (dashed lines) (twelve different areas are retained here). Curves correspond to averages from 8 h to 10 h. See text for further explanation.

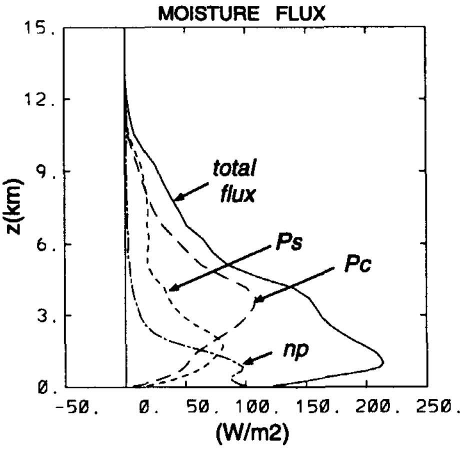

Figure 17. Moisture fluxes: total flux $c_p\pi_0\rho_0\overline{w\theta}^{\mathrm{T}}$ (solid line) and contributions of effective fluxes $(\sigma_i\overline{w}^i\left(\overline{\alpha}^i-\overline{\alpha}^{\mathrm{T}}\right)+\sigma_i\overline{w'_i\alpha'_i}^i)$ in the areas of convective precipitation A_{pc} (long-dashed line) and stratiform precipitation A_{ps} (short-dashed line) , and in the non-precipitating environment (dashed-dotted line) from 8 h to 10 h.

1 km (stage STG1 in particular) is now transported upwards. The importance of moisture transport is once again stressed by these profiles.

(*b*) *Restitution of the total vertical fluxes*

The total vertical flux of a quantity α over A_{T} can be seen as the sum of fluxes over different internal areas A_i ($\overline{w\alpha}^{\mathrm{T}}=\sum_i\sigma_i\overline{w\alpha}^i$, with $A_{\mathrm{T}}=\sum_i A_i$).

The contribution of each area A_i, in its turn, can be split into:

$$\sigma_i\overline{w\alpha}^i=\sigma_i\overline{w}^i\overline{\alpha}^{\mathrm{T}}+\left(\sigma_i\overline{w}^i\left(\overline{\alpha}^i-\overline{\alpha}^{\mathrm{T}}\right)+\sigma_i\overline{w'_i\alpha'_i}^i\right) \tag{12}$$

with primes indexed i denoting deviations from the average $\overline{\alpha}^i$ over A_i. The first term on the right-hand side is related to the mean vertical velocity $\overline{w}^i$ in A_i. It is much larger than the last two terms, as the domain average $\overline{\alpha}^{\mathrm{T}}$ (for $\alpha=\theta$ or q_{v}) is much larger than the deviations $\left(\overline{\alpha}^i-\overline{\alpha}^{\mathrm{T}}\right)$ (see section 4(d)). However, at the domain-scale this term is computed explicitly by the large-scale model, as we have: $\sum_i\sigma_i\overline{w}^i=\overline{w}^{\mathrm{T}}=w_{\mathrm{LS}}$. Hence it is more appropriate to retain only the sum of the last two terms in Eq. (12), which corresponds to the 'effective contribution' of fluxes in A_i to the total flux.

Figure 17 presents the total moisture flux and its decomposition into 'effective contributions' from A_{pc}, A_{ps} and A_{np}. Fluxes in clear sky and in anvils are negligible, and effective fluxes in A_{pc} are the most important above 3 km. However, shallow clouds are responsible for low-layer fluxes and stratiform precipitating regions contribute everywhere, with a maximum around 2 km due to new convective cells. In short, the total moisture flux is mainly explained by in-cloud effective fluxes, and the splitting into different types of clouds (shallow, convective and stratiform) shows that all of them contribute significantly to the total flux.

Returning to the domain-scale, the total flux can be split into two terms as follows:

$$\rho_0\overline{\alpha w}^{\mathrm{T}}=\sum_i\rho_0\overline{\alpha w}^i=\sum_i\rho_0\sigma_i\overline{w}^i\left(\overline{\alpha}^i-\overline{\alpha}^{\mathrm{T}}\right)+\sum_i\rho_0\sigma_i\overline{w'_i\alpha'_i}^i \tag{13}$$

The first term on the right-hand side corresponds to the contributions of mean fluxes at the area-scales, explained by mean profiles of α and mass fluxes, whereas the second term is associated with sub-area-scale fluxes.

For some parametrization schemes only two internal areas are considered (cloud and environment). Here an ensemble of 12 distinct areas has been used to perform this decomposition. It corresponds to the updraughts and downdraughts parts of the six basic internal areas defined in section 2(c). However, even with this fine-scale decomposition of the domain, the sum of the area-scale fluxes (Fig. 16, dashed lines) explains only $\frac{1}{3}$ to $\frac{1}{2}$ of the total flux. A cruder decomposition with only the six basic internal areas significantly degrades the estimation of the total flux ($\frac{1}{6}$ to $\frac{1}{4}$).

Hence significant convective fluxes occur on a very small scale, so that average profiles of vertical velocity, temperature and water vapour are not adequate for their estimation. This result agrees with observations of convective clouds discussed in Emanuel (1991): they 'reveal an extraordinary degree of inhomogeneity, with much of the vertical transport accomplished by subcloud-scale drafts'.

This is not, however, the usual hypothesis for convection schemes using bulk convective draughts, which also produce relatively high temperature and water vapour deviations. Our results suggest that a suitable way to express convective transport in a bulk-cloud model would be to take into account subcloud-scale transports. It raises a closure problem as relations still need to be estimated between area-scale characteristics and sub-area-scale fluxes.

7. CONCLUSION

In this study the thermodynamical impact of a cloud system, observed on 17 February 1993 in the western equatorial Pacific during TOGA-COARE, has been investigated using a cloud-resolving model. This case-study corresponds to the development during the night of convective lines, oriented approximately parallel to a moderate low-level shear. This type of system is very common over the western equatorial Pacific, and is characterized by the absence of large-scale ascent.

The three-dimensional simulation develops convection by itself, starting from small random perturbations of temperature, thus avoiding the artificial initialization by a cold or warm perturbation which is commonly used. A realistic simulation of a cloud population is obtained, including different types of clouds (shallow to deep), over 10 hours of its life cycle. During a first stage the boundary layer is built up, and then small cumuli appear at the top of the boundary layer but without generating precipitation. This stage is crucial to store moisture in the PBL so that the following stage is explosive. It corresponds to the sudden release of the energy through numerous convective clouds. Convection is mainly warm and cannot penetrate much higher than 8 km, but is very efficient at moistening the 1.5 to 5 km layer. The last, intensely convective, stage occupies the whole depth of the troposphere; it develops convective lines parallel to the low-level shear and generates icy anvils. At the same time shallow clouds develop, forced by lifting within the boundary layer induced by convective downdraughts.

The thermodynamical impact and statistical properties of the system have been analysed during the final stage, with a partitioning of the total domain into several (6 to 12) internal areas, including convective and stratiform precipitating areas as well as clear-sky columns.

Different behaviour of the vertical distribution of the apparent heat source Q_1 and apparent moisture sink Q_2 is obtained for this system, as previously found for other cloud ensembles (Johnson 1984; Lafore *et al.* 1988; Caniaux *et al.* 1994). At the domain-scale differences can be explained mainly by significant convective transport of moisture, as opposed to much weaker convective transport of heat.

An analysis of temperature deviations for the internal areas shows that the convective precipitation area is only slightly warmer than the other parts of the domain, in agreement with aircraft data analyses (Jorgensen and LeMone 1989; Lucas *et al.* 1994). Virtual liquid and solid potential temperature θ_{vl} (i.e. virtual potential temperature taking into account the water loading) deviations are still weaker, which means that the excess buoyancy in clouds is extremely small. The system develops under a density-equilibrium condition, involving both thermodynamics and microphysics through hydrometeor loading. Temperature deviations are also completely decoupled from vertical-velocity fields, unlike water vapour deviations which are positive in updraught layers and negative in downdraught layers.

The decomposition of thermodynamical budgets highlights the mechanisms of compensation occurring between the precipitating system and its environment. The latent-heat release in the precipitating part is approximately compensated by the mean vertical advection, so that the contribution of this area to the total warming is small. Most of the total warming occurs in the environment, through compensating subsidence.

Water vapour budgets are more complex to analyse, and show significant lateral exchanges. In particular, both low-level downdraughts in the precipitating system and the coexisting shallow clouds have a great impact on the budgets.

Finally, fine-scale analysis shows that convective fluxes occur at very small scales, so that average profiles of vertical velocity, temperature and water vapour are not adequate for their estimation. This result agrees with observations of convective clouds discussed by Emanuel (1991). It suggests that bulk-cloud models should take into account subcloud-scale processes. The next step of this study would be to evaluate the consequences of the different behaviour of an explicitly simulated cloud ensemble compared with a parametrized one, a strategy which has now become an important part of the Global Energy and Water Cycle Experiment Cloud System Study project (Moncrieff *et al.* 1997).

ACKNOWLEDGEMENTS

The authors are grateful to N. Asencio for very helpful computing assistance, to G. Caniaux for his information relative to microphysics parametrization and to T. Dore for his reading of the manuscript. The text was improved by the constructive comments and suggestions of P. Brown and an anonymous reviewer.

REFERENCES

Arakawa, A. and Schubert, W. H.	1974	Interaction of a cumulus cloud ensemble with the large-scale environment: Part I. *J. Atmos. Sci.*, **31**, 674–701
Balaji, V. and Redelsperger, J.-L.	1996	Sub-gridscale effects in mesoscale deep convection: initialisation, organization and turbulence. *Atmos. Res.* **40**, 339–381
Betts, A. K.	1990	Greenhouse warming and the tropical water budget. *Bull. Am. Meteorol. Soc.*, **71**, 1464–1467
Bougeault, P.	1985	A simple parameterization of the large-scale effects of cumulus convection. *Mon. Weather Rev.*, **113**, 2108–2121
Caniaux, G., Redelsperger, J.-L. and Lafore J.-P.	1994	A numerical study of the stratiform region of a fast moving squall line. Part I: general description and water and heat budgets. *J. Atmos. Sci.*, **51**, 2046–2074

Cess, R. D., Potter, G. L., Blanchet, J. P., Boer, G. J., Del Genio, A. D., Deque, M., Dymmikov, V., Galin, V., Gates, W. L., Ghan, S. J., Kiehl, J. T., Lacis, A. A., Le Treut, H., Li, Z.-X., Liang, X.-Z., McAvaney, B. J., Meleshko, V. P., Mitchell, J. F. B., Morcrette, J.-J., Randall, D. A., Rikus, L., Roeckner, E., Royer, J.-F., Schlese, U., Sheinin, D. A., Slingo, A., Sokolov, A. P., Taylor, K. E., Whashington, W. M., Wetheral, R. T., I. Yagai, I. and Zhang, M.-H. 1990 Intercomparison and interpretation of climate feedback processes in 19 atmospheric general circulation models. *J. Geophys. Res.*, **95,** 16601–16615

Chong, M. and Hauser, D. 1990 A tropical squall line observed during the COPT 81 experiment in West Africa. Part III: Heat and moisture budgets. *Mon. Weather Rev.*, **118,** 1696–1706

Emanuel, K. A. 1991 A scheme for representing cumulus convection in large-scale models. *J. Atmos. Sci.*, **48,** 2313–2335

Gamache, J. F. and Houze, R. A. 1982 Mesoscale air motions associated with a tropical squall line. *Mon. Weather Rev.*, **110,** 118–135

Gregory, D. and Miller, M. J. 1989 A numerical study of the parametrization of deep tropical convection. *Q. J. R. Meteorol. Soc.*, **115,** 1209–1241

Gregory, D. and Rowntree, P. R. 1990 A mass flux convection scheme with representation of cloud ensemble characteristics and stability-dependent closure. *Mon. Weather Rev.*, **118,** 1483–1506

Guichard, F., Redelsperger, J.-L. and Lafore, J.-P. 1996 The behaviour of a cloud ensemble in response to external forcings. *Q. J. R. Meteorol. Soc*, **122,** 1043–1073

Jabouille, P. 1996 'Organisation of convection observed during the TOGA-COARE experiment and its impact on surface fluxes'. Ph.D. dissertation, Université Paul Sabatier, Toulouse

Jabouille, P. and Redelsperger, J.-L. and Lafore, J.-P. 1996 Modification of surface fluxes by atmospheric convection as viewed from numerical simulation. *Mon. Weather Rev.*, **124,** 816–837

Johnson, R. H. 1984 Partitioning tropical heat and moisture budgets into cumulus and mesoscale components: implications for cumulus parameterization. *Mon. Weather Rev.*, **112,** 1590–1601

Jorgensen, D. P. and LeMone, M. A. 1989 Vertical velocity characteristics of oceanic convection. *J. Atmos. Sci.*, **46,** 621–640

Krueger, S. K. 1988 Numerical simulation of tropical cumulus clouds and their interactions with the subcloud layer. *J. Atmos. Sci.*, **45,** 2221–2250

Lafore, J.-P., Redelsperger, J.-L. and Jaubert, G. 1988 Comparison between a three-dimensional simulation and doppler radar data of a tropical squall line: transport of mass, momentum, heat and moisture. *J. Atmos. Sci.*, **45,** 3483–3500

Lin, X. and Johnson, R. H. 1996 Heating, moistening and rainfall over the Western Pacific Warm Pool during TOGA-COARE. *J. Atmos. Sci.*, **53,** 3367–3383

Lindzen, R. S. 1990 Some coolness concerning global warming. *Bull. Am. Meteorol. Soc.*, **71,** 288–299

Lipps, F. B. and Hemler, R. S. 1986 Numerical simulation of deep tropical convection associated with large-scale convergence. *J. Atmos. Sci.*, **43,** 1796–1816

Lord, S. J. 1982 Interaction of cumulus cloud ensembles with the large-scale environment. Part III: semi-prognostic test of the Arakawa-Schubert cumulus parameterization. *J. Atmos. Sci.*, **39,** 88–103

Louis, J.-F. 1979 A parametric model of vertical eddy fluxes in the atmosphere. *Boundary-Layer Meteorol.*, **17,** 187–202

Lucas, C., Zipser, E. J. and LeMone, M. A. 1994 Vertical velocity in oceanic convection off tropical Australia. *J. Atmos. Sci.*, **51,** 3183–3193

Moncrieff, M. W., Krueger, S. K., Gregory, D., Redelsperger, J.-L. and Tao, W.-K. 1997 GEWEX Cloud system study (GCSS) Working group 4: Precipitating convective cloud systems. *Bull. Am. Meteorol. Soc.*, **78,** 831–844

Morcrette, J.-J. 1991 Radiation and cloud radiative properties in the European Centre for Medium-Range Weather Forecasts forecasting system. *J. Geophys. Res.*, **96,** 9121–9132

Redelsperger, J.-L. and Lafore, J.-P. 1994 Non-hydrostatic simulations of a cold front observed during the FRONT 87 experiment. *Q. J. R. Meteorol. Soc.*, **120,** 519–555

Redelsperger, J.-L. and Sommeria, G. 1986 Three-dimensional simulation of a convective storm: sensitivity studies on subgrid parameterization and spatial resolution. *J. Atmos. Sci.*, **43,** 2619–2635

Siebesma, A. P. and Cuijpers, J. W. M. 1995 Evaluation of parametric assumptions for shallow cumulus convection. *J. Atmos. Sci.*, **52,** 650–666

Sommeria, G. 1976 Three-dimensional simulation of turbulent processes in an undisturbed trade wind boundary layer. *J. Atmos. Sci.*, **33,** 216–241

Sommeria, G. and LeMone, M. A. 1978 Direct testing of a three-dimensional model of the planetary boundary layer against experimental data. *J. Atmos. Sci.*, **35,** 25–39

Soong, S.-T. and Tao, W.-K. 1980 Response of deep tropical cumulus clouds to mesoscale processes. *J. Atmos. Sci.*, **37,** 2016–2034

Sui, C.-H., Lau, K. M., Tao, W.-K. and Simpson, J. 1994 The tropical water and energy cycles in a cumulus ensemble model. Part I: equilibrium climate. *J. Atmos. Sci.*, **51,** 711–728

Tao, W.-K. and Simpson, J. 1989 Modeling study of a tropical squall-type convective line. *J. Atmos. Sci.*, **46,** 177–202

Tao, W.-K. and Soong, S.-T. 1986 A study of the response of deep tropical cumulus clouds to mesoscale processes: three-dimensional numerical experiments. *J. Atmos. Sci.*, **43,** 2653–2676

Tao, W.-K., Simpson, J. and Soong, S.-T. 1987 Statistical properties of a cloud ensemble: a numerical study. *J. Atmos. Sci.*, **44,** 3175–3187

Tiedtke, M. 1989 A comprehensive mass flux scheme for cumulus parameterization in large-scale models. *Mon. Weather Rev.*, **117,** 1779–1800

1993 Representation of clouds in large-scale models. *Mon. Weather Rev.*, **121,** 3040–3061

Xu, K.-M. 1994 A statistical analysis of the dependency of closure assumptions in cumulus parameterization on the horizontal resolution. *J. Atmos. Sci.*, **51,** 3674–3691

1995 Partitioning mass, heat and moisture budgets of explicitly simulated cumulus ensembles into convective and stratiform components. *J. Atmos. Sci.*, **52,** 551–573

Xu, K.-M. and Arakawa, A. 1992 Semiprognostic tests of the Arakawa–Schubert cumulus parameterization using simulated data. *J. Atmos. Sci.*, **49,** 2421–2436

Xu, K.-M. and Emanuel, K. 1989 Is the tropical atmosphere conditionally unstable? *Mon. Weather Rev.*, **117,** 1471–1479

Xu, K.-M., Arakawa, A. and Krueger, S. K. 1992 The macroscopic behavior of cumulus ensembles simulated by a cumulus ensemble model. *J. Atmos. Sci.*, **49,** 2402–2420

Yanai, M., Esbensen, S. and Chu, J.-H. 1973 Determination of bulk properties of tropical cloud clusters from large-scale heat and moisture budgets. *J. Atmos. Sci.*, **30,** 611–627